Dielectric barrier discharge as bipolar ion source for aerosol charging: Application to filtration, thin film, and aerosol size measurement

Nicolas Jidenko, Rémi Mathon, Valentin Gérard, Abdul Malik Adédiran, Jean-Pascal Borra

Dielectric Barrier Discharge as bipolar ion source for aerosol charging: application to filtration, thin film, and aerosol size measurement

Nicolas Jidenko, Rémi Mathon, Valentin Gérard, Abdul Malik Adédiran and Jean-Pascal Borra
Laboratoire de Physique des Gaz et des Plasmas, CNRS, Université Paris-Saclay, F-91405 Orsay, France

Corresponding author: nicolas.jidenko@universite-paris-saclay.fr

Abstract. We have investigated the potentialities of dielectric barrier discharges (DBD) for aerosol electro-processing with a special focus on ion production and aerosol charging for deposition (filtration and materials) and aerosol measurement tools. The advantages and drawbacks of aerosol injection downstream or upstream of the discharge are compared according to the application. The main parameters that control ion production and transport are investigated based on post-discharge ion current measurements. Post-DBD aerosol chargers are compared for submicron particle size measurements based on aerosol bipolar charging and electrical mobility analysis. Finally, the principle of counterflow extraction of bipolar ion from an atmospheric pressure DBD is established from upstream measurements of positive and negative ion fluxes in air, without neither ozone (< 0.1 ppmv) nor nanoparticles.

Keywords: non-thermal plasma, dielectric barrier discharge (DBD), aerosol charging

1. Introduction

For the last three decades, dielectric barrier discharges (DBD) have been tested for many applications involving aerosol [1] (suspension of solid or liquid particles in a gas): the production of nanoparticles by nucleation of vapor produced by plasma surface-interaction [2, 3], the production of coatings, either homogeneous [4] or nanocomposite polymer thin film [5-8], the in-flight coating of nanoparticles for thermal stabilization of catalyzer [9], the electro-filtration [10], advantageously used as a self-cleaning filter [11] or the treatment of airborne virus [12, 13].

DBD consists of two metal electrodes with, at least, one dielectric barrier and one gas layer in between [14]. In air, at atmospheric pressure, the discharge mainly occurs as transient microdischarge –MD– (duration ~15–20 ns, diameter ~ 20–100 µm) distributed over the electrode surface [15]. These MD produce ions and electrons that undergo local electro-collection, within ns to µs in DBD [16, 17]. Most charges are collected on the dielectric surfaces, about only 10^{-4} % of the ions are measured downstream of the DBD [18]. During the ms transit time between dielectric materials, the electric drift of charges is due to Laplacian and surface electric fields as well as to space charge electric field [19-21].

Once injected in the DBD, aerosols are charged by the collection of gaseous ions or electrons[22]. The mechanisms of aerosol charging and the related charging laws are already defined versus particle diameter in unipolar clouds as well as in bipolar ion clouds [23]. Particles smaller than 100 nm are charged by the diffusion of ions. Particles larger than 500 nm are mainly charged by field charging when ions drift on the field lines intersecting the surface of the particle. In a unipolar ion cloud, the particle charge level depends on the size of the particle, the electric field, as well as the product of ion density (N_i, m^{-3}), and the transit time in this density (τ, s)[1]. In homogeneous bipolar ion clouds, aerosols of a given size reach a steady state charge distribution with a mean charge per particle depending on the ratio of positive to negative products of ion density by ion mobility ($N_{ion}{\cdot}Z_{ion}$ ratio) [24].

One promising application of DBD for aerosol charging relies on the bipolar charging required for aerosol size measurements. Particle size distributions are measured in the

submicron range by electrical mobility analysis that requires a bipolar ion source to control the charge distribution of particles with a mean close to zero, before mobility selection and particle counting [25]. Radioactive materials are used as bipolar ion sources but due to expensive safeguards and legal restrictions in some countries [26], neutralizers based on soft X-ray [27], UV[28] or based on electrical discharges [29-32] have been developed. More recently, dielectric barrier discharges (DBD) have been tested as a source of bipolar ions to charge aerosol injected in the discharge gap [20, 33, 34]. With no legal restrictions, lower cost than radioactive source and lifetime over 10 years, DBD neutralizers could be used for atmospheric and indoor monitoring of aerosol concentration and size. Nevertheless, the oxidation of measurement tools downstream of the discharge by chemical species produced in air still had to be addressed. This has first led us to propose to charge aerosols injected downstream a DBD fed with Nitrogen[35]. Going one step further, we present a more easy-to-use DBD neutralizer fed with air, as a clean ion source without oxidizing species.

The present work first aims to depict the production, transport, and losses of ions based on ion currents measurements downstream as well as upstream of the discharge. Starting with aerosol injected in the DBD, we depict aerosol charging and electro-collection of charged species in the gap as well as in post-discharge. Then, applications are presented in two parts depending on whether one seeks to collect aerosols in the DBD or to extract them from the DBD. Applications based on aerosol injection upstream or downstream of the DBD for aerosol charging devoted to aerosol size measurements are presented with a special focus on a new principle of counterflow extraction of bipolar ions from DBD. At last, the discussion focused on geometry and operating conditions of DBD according to the application, to highlight the respective interest and limits of upstream and downstream aerosol injections.

2. Experimental setup and methods

Figure 1 represents the experimental setup. Two main arrangements are used. To study the discharge and the post-discharge ions, dry and filtered air is injected in the DBD. To study aerosol properties after injection in or after the DBD, size, concentration, and charge level are measured.

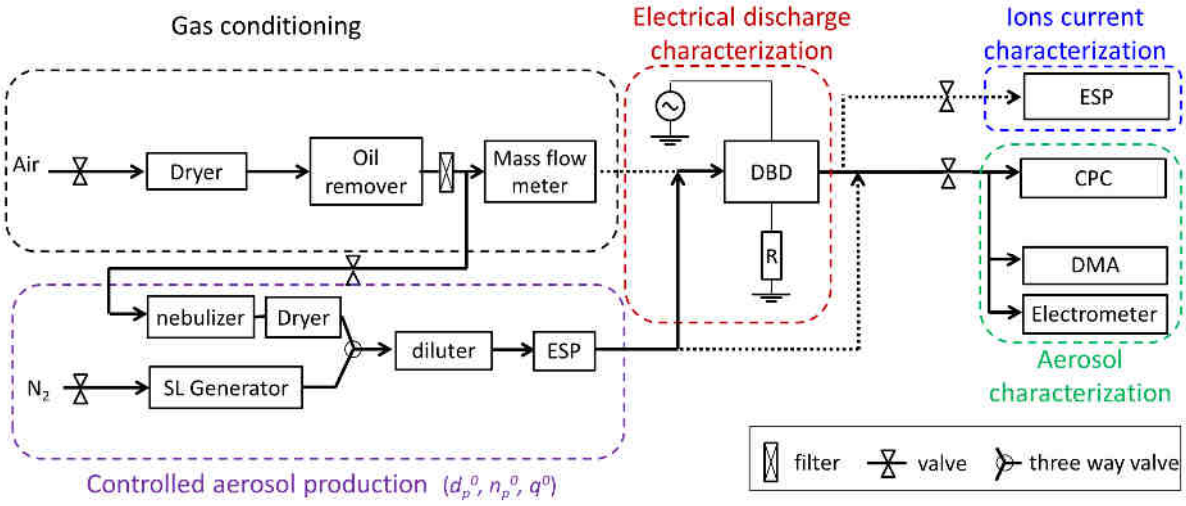

Figure 1. Experimental setup (CPC: condensation particle counter, DMA: Differential mobility analyzer, ESP: electrostatic precipitator)

The flow rate of dry and filtered air is regulated from 0.3 to 8 L min^{-1} by a mass flow controller. The pressure in the DBD reactor is kept constant at 1020 mbar +/- 2 mbar.

2.1. DBD arrangements

For the three arrangements, the metal electrodes are bars or rings with a diameter of 4 mm and the dielectric material is alumina (Al_2O_3, 96% purity).

For the plane-to-plane arrangement (cf. Figure 2a), two metal cylinders (length: $L_{electrode}$ = 30 mm) are laid on 0.5 mm thick alumina plates and covered by a silicon paste to prevent from electrical discharge around the metal electrodes. The distance between alumina plates (d_{gap}, referred as the discharge gap length) is controlled by metal spacers (0.5, 0.9, 1, 1.6, or 1.7 mm) and the gas injection section is 36 or 50 mm wide (L_{wall}).

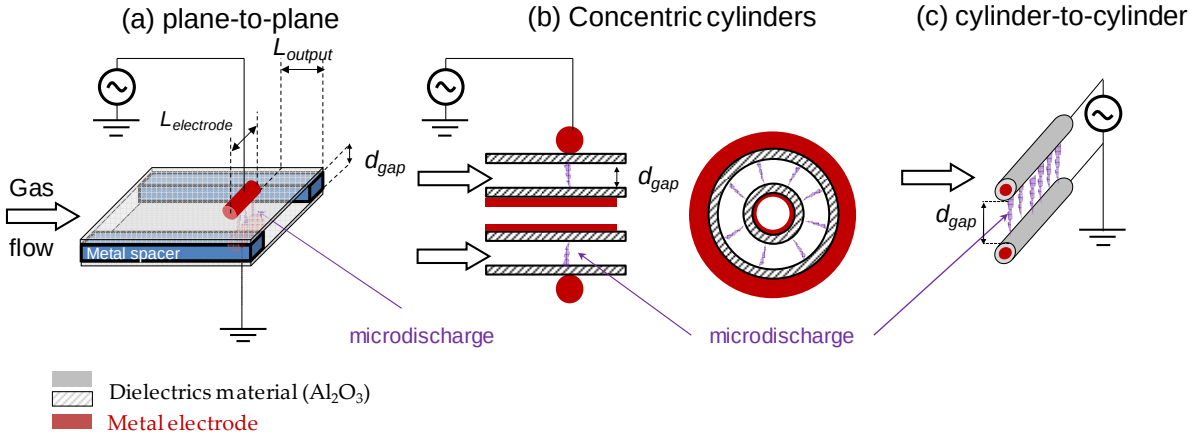

Figure 2. Discharge arrangements: (a) plane-to-plane (b) concentric cylinders (c) cylinder-to-cylinder

The length of the alumina plate downstream of the discharge (L_{output}) varies from 5 to 40 mm. The assembly is placed in an aluminum chamber (to enhance thermal exchanges with ambient air) with gas inlet and outlet. All the measurements, presented here, have thus been performed at least 30 minutes after any modification of the operating conditions to reach thermal equilibrium. The plane-to-plane arrangement is tunable and has been used to study the production of ions (cf. §3.2). The optimal discharge gap length in terms of maximal post-discharge ion density with a maximum peak-to-peak applied voltage of 20 kV is 1.5 mm, used for the two other arrangements.

For the arrangement with two concentric cylinders (Figure 2b), the central electrode is a tube inserted in the inner alumina cylinder , and the outer electrode is a ring. The alumina cylinders have external diameters of 12 and 16 mm. For the cylinder-to-cylinder arrangement (Figure 2c), two cylinders with a diameter of 6 mm are separated by a gap of 1.5 mm. For the three arrangements, the casings confining the gas flow are not represented for clarity reasons.

2.2. Electrical characterization of DBD

To compare discharge currents in different DBD, the measured current in the external circuit is corrected by the factor α [36-41] defined as:

$$\alpha = \frac{1}{1-\frac{C_{DBD}^{off}}{C_{alumina}}} \quad (1)$$

The capacitances of the DBD without plasma (C_{DBD}^{off} in F) and of the alumina ($C_{alumina}$ in F) are estimated with the smallest slope of the Lissajou's cycle [42, 43] using a capacitor instead of the measurement resistor R in Figure 1.

The discharge current is thus defined as:

$$I_{discharge} = 2F \cdot \alpha \left((q_{max} - q_{min}) - C_{DBD}^{off} \cdot V_{pp} \right) \quad (2)$$

where F is the applied voltage frequency, q_{max} and q_{min} the maximal and the minimal values of q on the Lissajou cycle, and V_{pp} the peak-to-peak applied voltage. α evolves from 1.2 to 1.6 for discharge gaps of 1.7 and 0.5 mm respectively.

2.3. Ion measurements

Since local positive and negative ion densities ${n_{ion}}^{+/-}$define both the net space charge affecting ion transport and the flux of ions of the surface of aerosol controlling aerosol charging, mean ion densities ${N_{ion}}^{+/-}$ are estimated from ion currents. In post-DBD, bipolar ions are separated by an electrostatic precipitator (ESP). Ion current collected on the grounded plate is measured by electrometers -Keithley 6010C or Keithley 6514 or Pegasor [44]. Positive and negative currents are measured one after the other. Significant efforts devoted to ensure the representativeness of ion measurements are detailed in §2.2 of supplemental information SI). The mean post-DBD ion densities are derived from ions currents, gas flow rate, and ions unit charge:

$${N_{ion}}^{+/-} = \frac{{I_{ions}}^{+/-}}{e.Q} \quad (3)$$

with I_{ions} the positive or negative ion current (A); e = 1.6×10^{-19} C the elementary charge and Q the gas flow rate (m^3 s^{-1}). The measured ion currents lie between pA to nA leading to ion densities between 10^{11} to 10^{14} m^{-3}.

2.4. Aerosol production and measurements

Monodisperse aerosols are produced by two generators. A Sinclair Lamer generator produces oil droplets between 400 nm to 900 nm. A nebulizer produces monodisperse aerosols made of polystyrene nanoparticles (PSL), with modal diameters between 20 nm to 200 nm.

Aerosol concentration is measured by a condensation particle counter (CPC). Aerosol size and charge distribution are measured by a differential mobility analyzer (DMA).

3. Ion production and transport

This section is devoted to summarize the main parameters that control the production and transport of ions. The ion current measured after the DBD (cf. §2.3) results from a competition between electric and hydrodynamic forces coupled with diffusion processes and ion-ion recombination. Most of the conclusions are based on the assumption that ion production downstream the discharge (by photo-ionization or by de-excitation of species in the gas or on the surface) can be neglected compared to the electro-hydrodynamic transport of charges from the MD developing in the gap, even if we cannot rule it out. The fact that similar post-DBD ion currents were measured with different post-discharge materials [18] supports the fact that surface chemical reactions and photoemission play a minor role.

3.1. Ion production

The electrical characterization of the DBD is the first step to identify the critical parameters for ion production (see Figure 3). The production of ions per second is proportional to the charge per microdischarge (MD) and the number of MDs per second. The charge per MD is proportional to the gap length and inversely proportional to the relative dielectric permittivity of the insulator [36, 45]. In plane-to-plane DBD with dry airflow, parametric influences of

overpressure, frequency, gas flow rate, gas temperature, and post-DBD tube material on post-discharge ion density and mobility have been reported for a given DBD geometry [18]. We focus here on the effects of the discharge gap length and the spatiotemporal distribution of the MDs as well as the transit time on post-DBD positive and negative ion currents and densities.

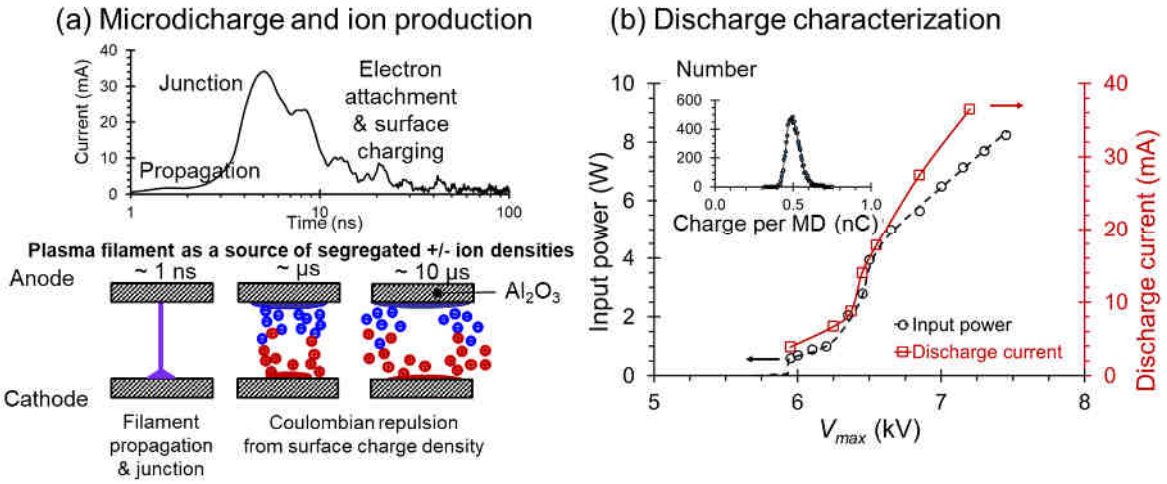

Figure 3. Electrical characterization of plane-to-plane DBD arrangement (a) microdischarge current with ion production for d_{gap} = 1.5 mm, $L_{electrode}$ = 3 cm, and (b) input power and discharge current as a function of the amplitude of the applied voltage (V_{max}) at F = 60kHz; the insert represents the distribution of charge per microdischarge

In Figure 3b, the different steps of a MD are presented. MD is initiated by the accumulation of positive space charge in volume [46], and by surface polarization, as detailed in point-to-plane[37] and planar DBDs[33] followed by a cathode-directed streamer that crosses the millimeter gap within 1 ns (the propagation) and leads to the formation of a conducting channel. From one half-period of the applied-voltage cycle (HP) to the other, MDs occur at the same place due to spatial memory related to the volume plasma and to the deposited surface charge that controls the MD shift in time [36, 37, 47]. Each MD can be considered as a transient and local source of electrons, ions, excited species, and UV and induces a current peak of 30 mA for a gap of 1 mm in the external circuit mostly due to electron flux in the gas. After the propagation of a MD, the polarization of the dielectric surfaces lowers the electric field that prevents from arcing and maintains some ions in suspension in the gas for µs [16, 47, 48]. The electric field in the discharge gap separates positive and negative ions in space until the inversion of the electric field due to surface polarization and applied voltage in the next half period.

Positive ions are produced in the MD by electron-molecule collision and photoionization whereas negative ions are produced by electron attachment on neutral gas molecule. Moreover, subcritical electron avalanches (with electrons number lower than Meek's criterion 10^8 and thus not followed by a streamer) [49] as well as, chemical reactions involving metastable and excited species could also account for ions production [50]. Gaseous ions measured downstream electrical discharges in air, at atmospheric pressure, are water cluster ions $M(H_2O)_n$ with M such as O_3^-, OH^-, CO^-, O_2^-, CO_3^-, NO_2^-, NO_3^-, HCO_3^- and H_3O^+, NO^+ or NO_2^+ [42, 51, 52], with a distribution of electrical motilities, detailed in [18].

3.2. Ion transport downstream the discharge

Bipolar ion transport and losses have been widely studied versus space charge, Laplace, and surface electric fields: without Laplace electric field [53-59] or with Laplace electric field [16,

[60-62]. Once produced, bipolar ions are collected to the walls by diffusion and electric drift, as well as neutralized by ion-ion recombination in volume. In most cases, diffusion and electrical drift parallel to the gas flow are assumed to be negligible compared to the gas velocity[63].

3.3. Gap length, applied voltage and MDs organization

Apart from the frequency presented in section 4, the discharge gap is the most critical parameter that controls post-DBD ion current as seen in Figure *4*b. Only negative ion currents are plotted as positive ion currents follow the same trends [18]. The spatial distribution of MDs in time and space evolves as depicted in inserts of Figure *4*a for different voltage ranges with related distributions of MDs (I, II, and III). The MDs distributions affect the efficiency of ion extraction defined as the ratio of I_{ion} over $I_{discharge}$ when ions are measured as close as possible to the discharge, as seen in Figure *4*b.

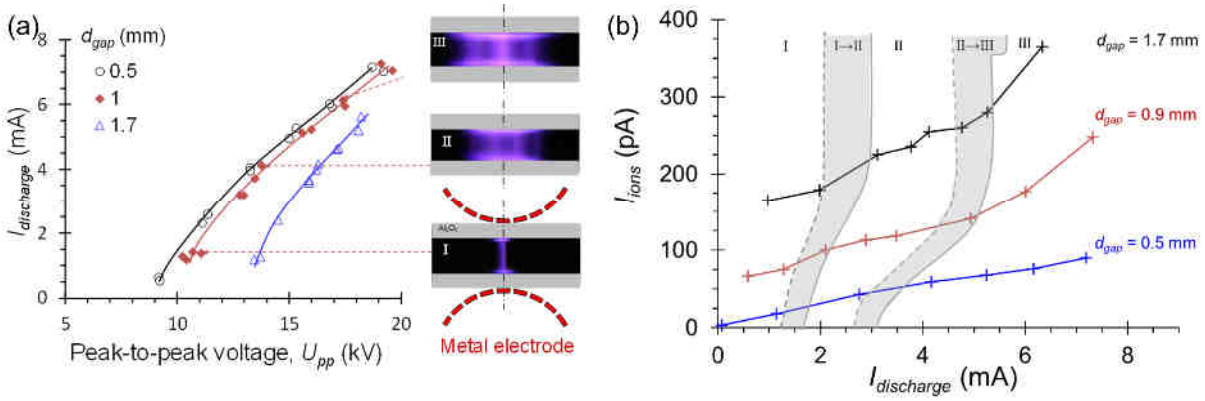

Figure 4. (a) Discharge currents as a function of applied voltage for d_{gap} of 0.5, 0.9, and 1.7 mm at 60 kHz for a gas flow rate of 4 L.min^{-1} and 3 photographs of the DBD at 10 kV, 12.7 kV, and 16.7 kV for the 0.9 mm gap DBD. (b) Downstream-DBD ions currents as a function of the discharge current $I_{discharge}$

Due to the cylindrical shape of metal electrodes, the Laplace electric field is not homogeneous in the discharge gap and leads to self-organizations of MDs that differs from those described in more homogeneous Laplace field in air for plane-to-plane electrodes rather than cylinder-to-cylinder [64-66]. MDs tend to line up in different planes defined as curtains [21].

At low applied voltage, only one curtain of MDs is observed where the Laplace field is maximum in the plane of symmetry. Then, at intermediate applied voltage, two curtains are observed on both sides of the plane of symmetry. The distribution of MDs on two curtains increases the number of MDs with the maximal distance between adjacent MDs. At last, for larger applied-voltage, three curtains are observed. The transitions between the different numbers of MD curtains extend over voltage ranges that depend on the discharge gap length. It has to be underlined that the distribution of charge per MD is unimodal only with one MD curtain. The increase in the number of MDs per period leads to higher post-discharge ion currents but reduces the ion extraction efficiency.

3.4. Transit time

To identify the dominant mechanisms of ion losses, post-DBD ion currents (I_{ion}) are measured for different transit times and compare to calculations as detailed in the §2.1 of SI. To summarize, ion losses depend on the considered volume. Electro-collection is dominant in the discharge volume (gas volume between the metal electrodes) and in the inter-alumina volume after the discharge. In the post-alumina volume, the reduction of ion densities is due to ion-ion recombination[35] (cf. §3.3 of SI). The transit time is adjusted by the flow rate, the length of the inter-alumina volume (L_{output} cf. Figure 3) as well as the length of the post-alumina

volume. As expected, the most critical transit time is the inter-alumina one which should be as short as possible to increase post-discharge ion densities (10 times higher at 9 mm from the discharge than at 17 mm, cf. Figure 5).

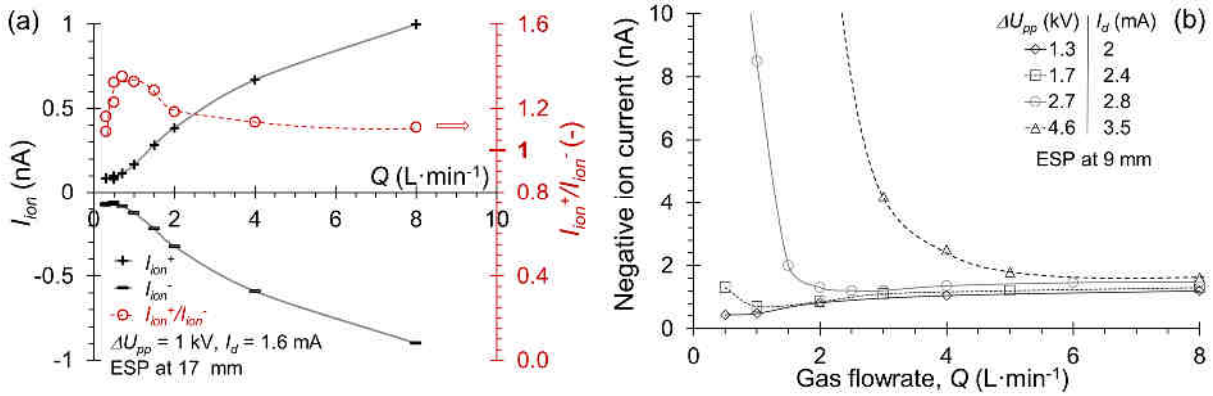

Figure 5. Post-DBD ion currents versus air flow rate for the 1.6 mm gap DBD, with L_{output} = 5 mm (a) for ΔU_{pp} = 1 kV, with ESP at 17 mm from DBD after a volume of 4 cm^{-3} and transit time from 30 ms to 0.9 s, I_d = 1.6 mA and (b) negative ion currents for ΔU_{pp} = 1.3, 1.7, 2.7 and 4.6 kV with ESP at 9 mm from DBD after a volume of 1.4 cm^{-3} and transit time from 10 to 300 ms.

Positive and negative ion currents follow the same trends with an excess of positive ions that can be tuned by the gas flow rate (cf. I_{ion}^+/I_{ion}^- in Figure 5a) and applied voltage (Figure 5b).

Positive to negative ion currents ratio I_{ion}^+/I_{ion}^- is correlated to aerosol mean charge [35, 67] and gives the dominant mechanism of ion losses. Recombination or/and Brownian diffusion control ion losses if I_{ion}^+/I_{ion}^- is higher than 1 and increases with the transit time. If the ratio I_{ion}^+/I_{ion}^- tends to 1 electrostatic repulsion is dominant. In Figure 5(a), the non-monotonous evolution of I_{ion}^+/I_{ion}^- shows that the dominant mechanism of ion losses depends on the gas flow rate range and the related distribution of ion clouds.

At gas velocity higher than 1 m s^{-1} (5 L min^{-1}) in the DBD, ion-ion recombination controls the decrease of ion densities a few tens ms after dielectric materials proving that bipolar ions are homogenously distributed in space.

Below 0.2 m s^{-1} (1 L min^{-1}), post-DBD ion densities are up to 10 times higher than above 1 m s^{-1} due to the laminar gas flow regime, with a higher temperature gradient and ion density gradient. Ion densities decrease less than expected by recombination proving that bipolar ions are partly separated in space (cf. §3.3 of SI).

The length of the alumina plate in post-discharge is an efficient way to control post-DBD ion currents. Depending on the targeted application, post-DBD ion currents up to a few nA can be achieved using an alumina length of a few millimeter or three orders of magnitude smaller with an alumina length of a few centimeters. The increase of the discharge gap length favors ion extraction from the discharge and limits ion losses in the post-discharge inter-alumina volume. To enhance post-DBD ion current, a discharge gap larger than 1.5 mm and applied-voltage frequency larger than 30 kHz lead to ion density larger than 10^{12} m^{-3}.

Despite reduced yield, as only 10^{-6} % of the charges are extracted from the discharge gap, DBD can thus be designed to favor an efficient transport of bipolar ion clouds with reduced losses compared to self-repulsion of unipolar ion cloud or ion recombination in homogeneous bipolar ion cloud (cf. §3.5).

3.5. Counter flow ion extraction

A counter flow-DBD ion source has been tested to charge aerosol upstream of the DBD as detailed in section 5.2 [68]. A flow of clean air in the opposite direction to the flux of ions to separate them from the discharge effluents: ozone, nitrogen oxides, and nanoparticle (cf. Figure 6). The arrangement with concentric cylinders is polarized by a 60 kHz sinusoidal voltage and an ion trap is used as ESP to measure post-DBD ion current (cf. Figure 6a). Average plasma power *P* and discharge current I_d follow the same trend as the voltage (not shown) and depend on the number of MDs per period and on the charge per MD of about 0.5 nC. The I-V characteristics of the ESP proves that all ions are collected above 1 kV (cf. Figure 6b). Due to the faster collection of electrons more mobile than ions, positive ions are in excess in the gap and downstream the DBD; the I-V characteristics of the ESP is thus shifted to positive values of ion trap current.

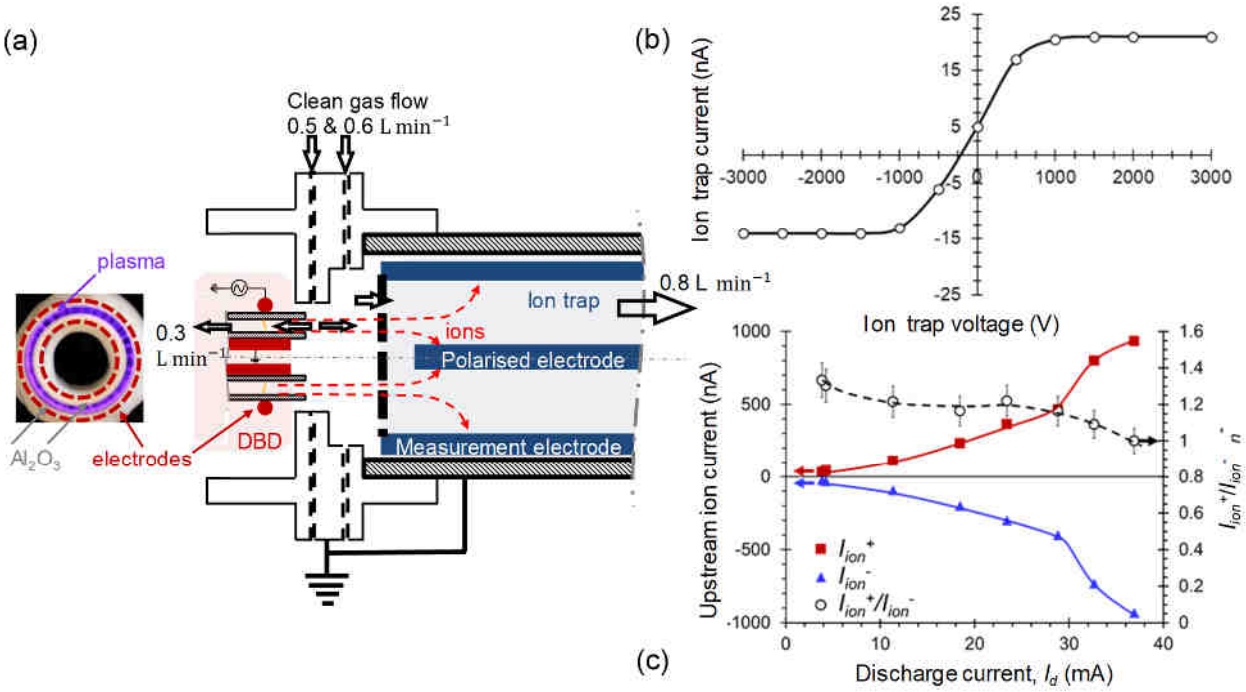

Figure 6.Counterflow-DBD ion characterization in cylinder-to-cylinder arrangement, (a) scheme of the DBD with a photograph of the DBD with sub-second aperture durations (b) I-V characteristics of the ion trap for a DBD voltage of 6 kV, Z_i^+/Z_i^- is estimated to 0.9 from the slopes, assuming the same positive and negative ion densities, and (c) upstream ion currents and positive-to-negative ion currents ratio as a function of the discharge current I_d. Assuming I_{ion}^+/I_{ion}^- equal to N_i^+/N_i^- at the entrance of the neutralizer, positive to negative ion currents ratio is about 1.2 for discharge current between 10 and 25 mA which leads to a $N_i \cdot Z_i^{+/-}$ ratio of 1.1.

Despite the gas flow injected in the discharge gap, ions are detected upstream (cf. Figure 6c). Diffusion and/or electrostatic processes are thus efficient to transport ions in the opposite direction to the gas flow. Thermal and ion density gradients as well as electrostatic repulsion of unipolar ions from the polarized feet of MD with opposite polarities (positive ions at the cathode side and negative ones at the anode) contribute to the ion transport.

Moreover, the production of separated unipolar ion clouds by plasma filaments in an AC electrical field limits ion-ion recombination. This mechanism of consumption of bipolar ions in volume, for densities larger than 10^{12} m^{-3} is thus less active than in homogenously mixed bipolar ion cloud leading to an efficient electrostatic transport of bipolar ions in DBD (cf. §3.3 of SI).

4. Injection of aerosol in DBD

The injection of aerosol in DBD modifies the electrical characteristics of the MD depending on aerosol size and concentration mainly due to aerosol space charge [10, 69, 70]. Moreover, the collection of aerosol on dielectric surfaces increases the surface conductivity that reduces discharge current with time [11].

Once aerosols are charged in a DBD, electrical forces are dominant compared to gravity and thermophoresis and thus control the trajectories of particles. The kinematics of aerosol in DBD have been treated in different works [19, 20, 71]. The applied voltage and frequency control the oscillation of the charged species (electron, ion, and aerosol) depending on their electrical mobility and thus the collection efficiency in the DBD. For aerosol, the location of the particle when the particle collects charges affects the trajectory. It has to be noticed that MDs increase the collection by a few tens of percent due to surface polarization as well as turbulences [20].

DBDs are operated at frequencies lower than 10 kHz to promote electro-deposition on surfaces and at higher frequencies to limit collection.

4.1. Applications with electro-collection at low frequency

DBDs have been tested from air quality applications as electro-filters for aerosol filtration [10, 11, 72] and more recently for airborne virus treatment [12]. Ionizing properties of plasma are used to charge and collect aerosol at low frequency (a few kHz). Reactive properties are used to destroy the collected combustion-like aerosol produced by DBD for VOC abatement or to inactivate viruses at high frequency (a few tens of kHz).

Nanocomposites thin films consist of nanoparticles embedded in a matrix. Three main methods are used to form the nanocomposite films.

Only precursors can be injected in the DBD to form both nanoparticles and film. As the charging by collection of ions is efficient only for particles larger than a few nanometers, the transit time has to be larger in the DBD longer than the times of vapors formation, nucleation and growth above the minimum size to get charged [73]. Hence, the electro-collection of particles on surfaces is used for thin film deposition in DBD with a frequency of a few kHz.

Nanoparticles and precursors can be injected in the DBD to produce the composite for hydrophobic surface [6], wood treatment [74]. A compromise has to be found as the growth rate of film formation increases with frequency whereas nanoparticle density decreases [5]. Amplitude and frequency modulations of the voltage applied onto the electrode overcome this limit and lead to homogeneous film growth] [71, 75].

This method has been used to coat agglomerated metal nanoparticles with thermo-stable SiO_x limiting sintering at high temperature to keep high active surface of catalyst agglomerates. Nevertheless, the injection of both particle and precursor downstream of the discharge prevents from the collection of aerosol inducing discharge destabilization and the destruction of precursor with loss of functionality [9].

4.2. Ions sources without electro-collection at high frequency

DBDs have also been tested as a source of bipolar ions to charge aerosol injected in the discharge for aerosol measurement tools [1, 20, 33, 34, 76]. Due to the excess of positive ions in the gap, the net charge of aerosol downstream the DBD is positive. Charge distribution after a bipolar ion source such as radioactive one has a Gaussian shape (cf. Figure 7b for Krypton source). The charge distribution of aerosol measured just after the DBD presents a positive mode and a negative mode depending on particle size as shown, in Figure 7, for 102 nm

particles [22, 77]. These two modes are due to the separation of positive and negative ions clouds in the discharge especially on both sides of MD.

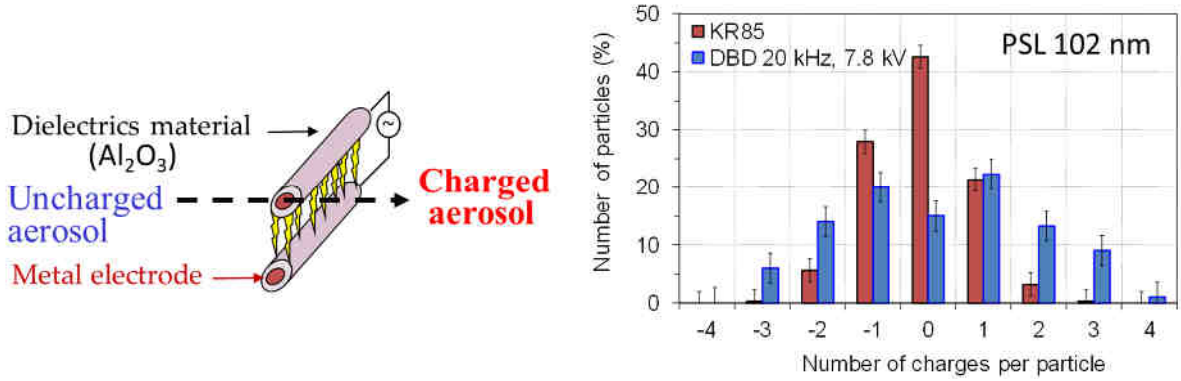

Figure 7. Schematic of aerosol charger with aerosol injection in the DBD and charge distribution of latex particle (PSL) measured downstream the DBD

The choice of 20 kHz is the result of a compromise between better aerosol extraction at higher frequency and higher power consumption inducing higher gas temperature that can alter aerosol properties (size, shape crystalline structure, and functional properties) due to evaporation, melting, or sintering.

It has to be noticed that the presence of ions downstream of the discharge, leads to the evolution of the charge distribution that tends to reach a Boltzmann distribution with time. Therefore, to obtain an ion source insensitive to aerosol properties, to prevent discharge from destabilization related to electro-collection of the aerosol in the discharge gap as well as modification of aerosol properties, aerosol can be charged after the DBD (cf. section 5). Ions can thus be blown from the discharge gap by a gas flow and mixed with aerosol downstream the gap if a frequency higher than 20 kHz is imposed to extract ions from the discharge, as detailed in the following section.

5. Post-DBD charging for aerosol measurements

In the submicron range, particle size distributions are measured using electrical mobility analysis. Scanning mobility particle sizers (SMPS) classify particles according to their electric mobility. Then, classified particles are counted with a condensation particle counter (CPC). To determine the initial particle size distribution from the measured mobility distribution of aerosols, data inversion requires to control the charge distribution of the aerosol upstream of the mobility classifier. To do so, bipolar diffusion chargers, also known as neutralizers, are used, where particles are introduced into an ionization chamber that contains ions of both polarities[25]. Radioactive material, soft X-ray [27], UV [28] or corona discharges [29-32], and DBD [20, 33, 34] have been developed to neutralize aerosol.

To ensure aerosol neutralization (i.e. to reach steady state bipolar charge distribution with a net charge close to zero), two conditions must be fulfilled in homogeneously mixed positive and negative ions. The $N_i \cdot \tau$ product should be higher than 6×10^{12} m^{-3} s with τ the transit time of aerosol in the ion density N_i that should be 10 times higher than aerosol concentration for aerosol larger than 20 nm [63, 78]. The $N_{ion}^+ Z_{ion}^+ / N_{ion}^- Z_{ion}^-$ ratio controls the mean charge per particle [79] with Z_i the mean ion electrical mobilities of ions. This ratio should be 0.87 [80], to use the current data treatment from mobility spectra to size distribution or the data treatment has to be adapted. In post-DBD, positive and negative ions are homogenously distributed, the ratio Z_{ion}^+ / Z_{ion}^- can be calculated from ion mobility measurements and lies in the range of 0.6 to 1.05 depending on operating conditions [18]. In post-DBD, the electric field is negligible

I_{ion}^+/I_{ion}^- is thus a good estimation of N_{ion}^+/N_{ion}^-. Z_{ion}^+ and Z_{ion}^- are measured by mobility measurements to define the $N_{ion}{\cdot}Z_{ion}$ ratio. It has to be underlined that in post-DBD, both Z_{ion}^+/Z_{ion}^- (due to ion ageing) and N_{ion}^+/N_{ion}^- (due to losses related to ion mobility) evolve along the post-discharge; nevertheless the $N_{ion}{\cdot}Z_{ion}$ ratio at the entrance of the charging volume can be used as an indicator of aerosol charging conditions.

5.1. Post-DBD neutralizers with a downstream injection of aerosols

An alternative to radioactive aerosol neutralizers for submicron particle size measurements by mobility analysis has been evaluated by Mathon et al. [81]. The initial ratio of positive and negative ion currents controlled by the DBD voltage leads to a tunable mean charge of aerosol in this post-DBD bipolar charger. As expected from Gunn's law, the mean charge and the variance are proportional to particle diameter above 50 nm and independent of the aerosol concentration up to $6{\cdot}10^{12}$ m^{-3}. The size distributions measured with a radioactive neutralizer ^{85}Kr (74 MBq) and the post-DBD neutralizer present the same modal diameters and a maximal overestimation of the total concentration of 10 %, for aerosol from 15 to 730 nm with concentrations up to $6{\cdot}10^{12}$ m^{-3}.

To prevent from corrosion of aerosol tools downstream DBD due to oxidizing species such as ozone or singlet oxygen, nitrogen injection in the DBD gap has also been tested. Despite obvious modifications of post-DBD ion mobilities from air to nitrogen, this post-DBD aerosol charger can be used, as currently available ^{85}Kr or X-rays neutralizers, for submicron-sized distribution measurements with stable operating conditions.

5.2. Counterflow ion extraction for upstream-DBD neutralization

To overcome the main drawback of DBD neutralizer (oxidizing species downstream of the DBD that alters the aerosol measuring tools), the principle of a post-DBD aerosol neutralizer with counterflow extraction of bipolar ion is established from aerosol mobility measurements. Bipolar ions are extracted from Dielectric Barrier Discharge (DBD) against the airflow injected in the gap, to be mixed upstream of the DBD with the sampled aerosol flow. This counterflow transport of bipolar ion first lies on electrostatic repulsion of unipolar ion clouds, and then mixed by diffusion into a necessarily homogeneous bipolar ion cloud to achieve the measured expected bipolar mobility distributions. Operating conditions for aerosol neutralization are defined from positive and negative ion fluxes, with respect to charging conditions ($N_i{\cdot}Z_i^{+/-}$ ratio). Similar aerosol size distributions are measured by mobility analysis with the DBD neutralizer and the reference one (^{85}Kr), with the same modal diameter and a maximal 15 % overestimation of the total concentration. The principle of this counterflow-DBD neutralizer is suitable for aerosol size measurements without oxidation of mobilimeter and particle counters nor artifact nanoparticles, as a reliable, long-life, and low-maintenance plasma ion source even in air.

At 6.5 kV (I_d = 10 mA), upstream ion densities at the entrance of the neutralizer and $N_i{\cdot}\tau$ product are estimated to be $5{\times}10^{12}$ m^{-3} and $3{\times}10^{12}$ m^{-3} s^{-1} respectively. In this condition, selected for neutralization, comparative tests of aerosol sizing with ^{85}Kr and counterflow-DBD neutralizers show similar size distributions with the same diameter modes (cf. Figure 8).

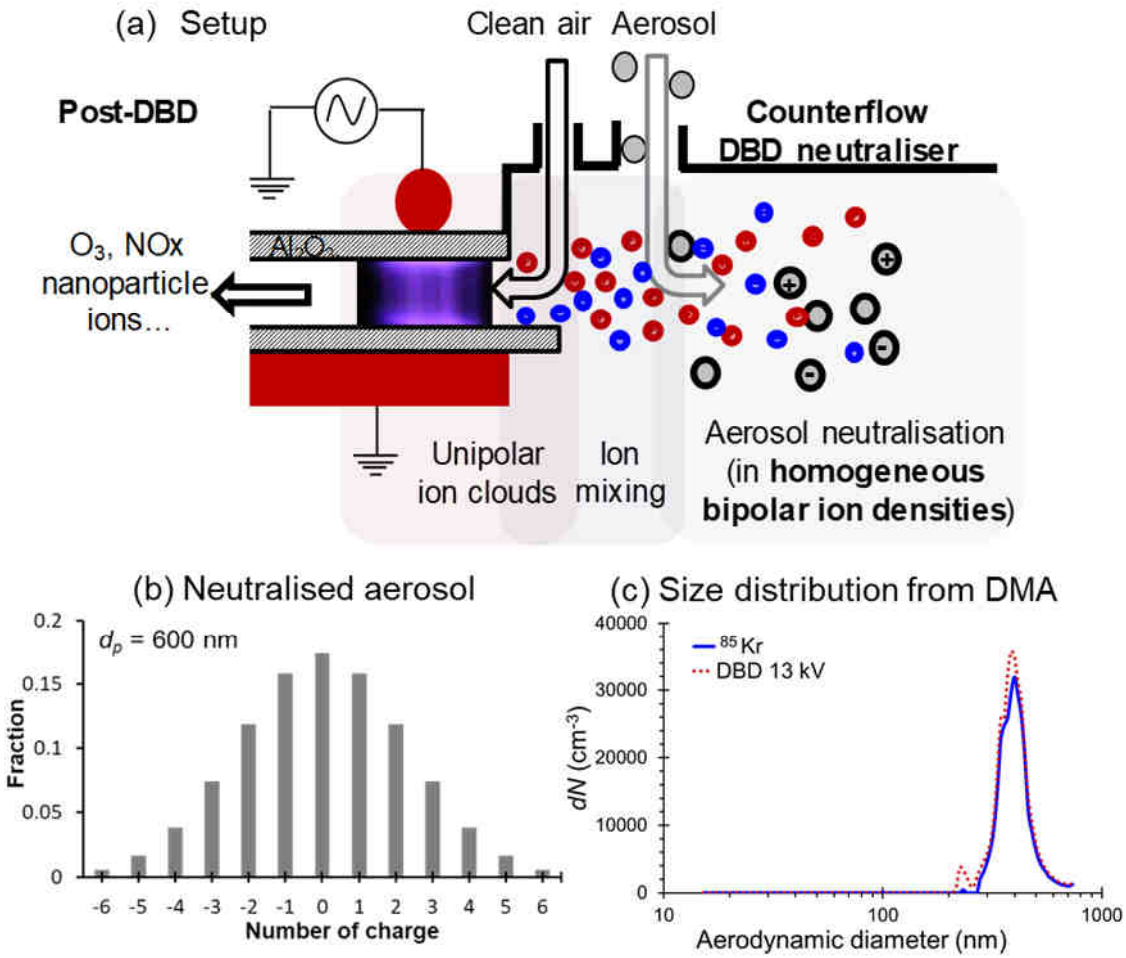

Figure 8. Comparison of neutralizers (^{85}Kr as a reference and counterflow-DBD): (a) electrical mobility spectra of positive particle and (b) size distribution after the correction of the charged fraction, both measured with a differential mobility analyzer (SMPS 3071 TSI Inc with Q_{sheath} = 3 L min^{-1} and $Q_{aerosol}$ = 0.3 L min^{-1}) for a counterflow-DBD neutralization time of 1 s at 0.8 L min^{-1}, V_{max} = 6.5 kV, I_d = 10 mA, aerosol concentration of 4×10^5 cm^{-3}

As expected, the higher $N_i \cdot Z_i^{+/-}$ ratio measured upstream of the DBD than the reference ^{85}Kr source, induces higher fractions of positively charged particles. This excess leads to an overestimation of total aerosol concentration of 15% that can be corrected by adapting the charged fraction in the data inversion algorithm.

This low-cost counterflow-DBD neutralizer can be used for submicron-sized aerosol neutralization, as currently available ^{85}Kr or X-rays neutralizers, without ozone nor nanoparticle from the DBD. Charge distributions of particles in the submicron range were reproducible with the standard deviation expected from theory. Aerosol losses in the neutralizer are lower than 95% for particles larger than 100 nm. This counterflow-DBD neutralizer is stable on large ranges of applied voltage and discharge current. Current studies aim to achieve steady state charge distribution for smaller particles and higher aerosol concentration as confirmed by preliminary results with different operating conditions of the plasma.

6. Discussion on DBD arrangement and operating conditions

Each of the three DBD arrangements has advantages. The plane-to-plane arrangement is simple and tunable. The arrangement with concentric cylinders is compact and suppresses the edge effects, whereas the cylinder-to-cylinder arrangement is optimal for aerosol injection in the DBD with a limited collection of aerosol.

As far as possible, aerosol injection in the DBD should be avoided to prevent the discharge evolution and destabilization with aerosol deposition in the DBD. Post-DBD reactivity or charging is to be favored as chemical species and charged species can be extracted from the discharge. Nevertheless, electro-filtration or thin film deposition requires to inject aerosol in the DBD that involves to characterize the influence of aerosol on the electrical discharge characteristics depending on the size, the concentration, the dielectric permittivity and the chemical nature of aerosol as well as to characterize the time evolution of the discharge with the aerosol deposition.

Post-DBD charging prevent from aerosol losses and aerosol modification with temperature and chemical reactions, in that respect counterflow is optimal even if the ion concentration is at least one order of magnitude lower than downstream the DBD.

To extract ions from the discharge, a frequency of the applied voltage above 30 kHz and a minimal length of dielectric material downstream of the discharge are the two main parameters to take into account.

All these considerations are essential to develop devices based on DBD for aerosol measurement of concentration, size, or nature. Moreover, these considerations can be useful for ongoing development on (i) plasma-surface interaction such as DBD treatment of seeds, biofilm, or surface decontamination, or (ii) plasma-liquid spray interaction such as water depollution of antibiotics and drugs and for the production of “activated water” to clean and decontaminate food and any surface.

7. Conclusions

The plasma filaments in Dielectric Barrier Discharges can be considered as local and brief sources of bipolar ions that can be transferred to post-discharge within the gas flow downstream the DBD as well as upstream the DBD. DBDs are thus a user-friendly, low cost and tunable bipolar ion source that can be used to neutralize charged surfaces, powders, or aerosols. The presence of charged species in the DBD exhaust gas flow, for frequencies above 30 kHz) has to be addressed, for instance by simple post-discharge arrangements with chosen materials to control heat exchanges and post-discharge electric fields by surface potentials, when DBDs are used for surface treatment or aerosol processes.

To optimize such a bipolar ion source at atmospheric pressure for aerosol neutralization, ion measurement protocols have been developed. The production of ions per second depends on the charge per MD and the number of MDs per second. The transport and losses of ions are controlled by an electro-hydrodynamics competition, as well as ion-ion recombination and diffusion. At low gas velocity (v_{gas} < 0.2 m s^{-1}), more laminar gas flow and enhanced heat and mass transfers lead to higher post-discharge ion densities than at gas velocity higher than 1 m s^{-1}. The spatio-temporal distribution of MDs plays a major role in ion transport due to electrostatics repulsions at the feet of the MD and diffusion related to density and temperature gradients as proven by the evolution of post-DBD ion current with the number of MD curtains controlled by the shape of the metal electrode and the applied-voltage.

In the discharge and the post-discharge inter-alumina volumes, ion densities are controlled, at first order, by electro-precipitation. In the post-alumina volume, positive and negative ion

densities are controlled by ion recombination and, to a lesser extent, by self-repulsion for positive ions in excess.

DBD can be used as a charger of aerosols in the discharge or in post-discharge. Charged aerosols (droplets, nanoparticles, or micronized particles) can then be deposited on the surface for filtration, composite nanomaterial, or focused deposition for coatings. Bipolar coagulation can also be used for nanoparticle assembly or micro-reactivity using droplets. One promising application is the counterflow ion extraction as a clean source of bipolar ions without oxidative specie nor nanoparticle from the DBD, suitable for aerosol size measurements.

Funding: All experimental studies have been performed at LPGP of CNRS-Université Paris Saclay and were supported by Palas GmbH [UMR8578/139172] and RAMEM [UMR8578/043277].

References

[1] Borra J P *Journal of Physics D: Applied Physics* 2006 **39** R19-R54
[2] Borra J P, Jidenko N, Hou J, et al. *Journal of Aerosol Science* 2015 **79** 109-125
[3] Jiang L, Li Q, Zhu D, et al. *Aerosol Science and Technology* 2017 **51** 206-213
[4] Borra J P, Valt A, Arefi-Khonsari F, et al. "Polymer surface processing by atmospheric pressure DBD for post-discharge grafting of washing-resistant functional coatings" In: T. Chandra, N. Wanderka, W. Reimers and M. Ionescu, eds. *Thermec 2009, Pts 1-4* 2009:524-529.
[5] Nadal E, Milaniak N, Glenat H, et al. *Nanotechnology* 2021 **32**
[6] Fanelli F, Mastrangelo A M and Fracassi F *Langmuir* 2014 **30** 857-865
[7] Santos B, Cacot L, Boucher C, et al. *Plasma Sources Science and Technology* 2019 **28** 045002
[8] Borra J-P, Valt A, Arefi-Khonsari F, et al. *Plasma Processes and Polymers* 2011 **9** 1104-1115
[9] Post P, Jidenko N, Weber A, et al. *Nanomaterials* 2016 **6** 91
[10] Dramane B, Zouzou N, Moreau E, et al. *Journal of Electrostatics* 2009 **67** 117-122
[11] Jidenko N and Borra J P *Journal of Hazardous Materials* 2012 **235** 237-245
[12] Xia T, Yang M, Marabella I, et al. *Journal of Hazardous Materials* 2020 **393** 122266
[13] Stancampiano A, Gallingani T, Gherardi M, et al. *Applied Sciences* 2019 **9** 3861
[14] Kogelschatz U, Eliasson B and Egli W "Dielectric-barrier discharges. Principle and applications" *XXIIIrd International Conference on Phenomena in Ionized Gases*. Toulouse, France: E D P Sciences 1997:47-66.
[15] Kogelschatz U *Plasma Chemistry and Plasma Processing* 2003 **23** 1-46
[16] Xu X D P and Kushner M J *Journal of Applied Physics* 1998 **83** 7522-7532
[17] Höft H, Becker M M and Kettlitz M *Physics of Plasmas* 2016 **23**
[18] Bourgeois E, Jidenko N, Alonso M, et al. *Journal of Physics D: Applied Physics* 2009 **42** 205202
[19] Zouzou N and Moreau E *Journal of Physics D-Applied Physics* 2010 **44**
[20] Jidenko N and Borra J-P *J. Phys D.: Apply Phys* 2005 **38** 617-620
[21] Mathon R, Jidenko N and Borra J P "Bipolar ions extraction from dielectric barrier discharge" *Gas Discharge* Orléans France 2014.
[22] Borra J P *Plasma Physics and Controlled Fusion* 2008 **28** 124036

[23] Fuchs N A *Pure and Applied Geophysics* 1963 **56** 185-193
[24] Nishida R T, Johnson T J, Hassim J S, et al. *Acs Sensors* 2020 **5** 447-453
[25] Knutson E O and Whitby K T *Journal of Aerosol Science* 1975 **6** 443-451
[26] Kallinger P and Szymanski W W *Journal of Nanoparticle Research* 2015 **17** 171
[27] Lee H M, Soo Kim C, Shimada M, et al. *Journal of Aerosol Science* 2005 **36** 813-829
[28] Li L and Chen D-R *Journal of Aerosol Science* 2011 **42** 87-99
[29] Adachi M, Okuyama K and Kousaka Y *Journal of Chemical Engineering of Japan* 1983 **16** 229-235
[30] Romay F J, Liu B Y H and Pui D Y H *Aerosol Science and Technology* 1994 **20** 31 - 41
[31] Han B, Hudda N, Ning Z, et al. *Journal of Aerosol Science* 2009 **40** 285-294
[32] Qi C and Kulkarni P *Aerosol Science and Technology* 2013 **47** 81-92
[33] Kwon S B, Fujimoto T, Kuga Y, et al. *Aerosol Science and Technology* 2005 **39** 987 - 1001
[34] Wild M, Meyer J and Kasper G "Evaluation of a Drained DBD Electrode Apparatus for Nano-Particle Charging" *European Aerosol Conference 2007*. Salzburg 2007:Abstract T05A009.
[35] Mathon R, Jidenko N and Borra J-P *Aerosol Science and Technology* 2016 1-10
[36] Jidenko N, Petit M and Borra J-P *J. Phys D.: Apply Phys* 2006 **39** 281
[37] Petit M, Jidenko N, Goldman A, et al. *Review of Scientific Instruments* 2002 **73** 2705-2712
[38] Zoran F and John J C *Journal of Physics D: Applied Physics* 1997 **30** 817
[39] Pipa A V, Koskulics J, Brandenburg R, et al. *Review of Scientific Instruments* 2012 **83**
[40] Manley T C *Transactions of The Electrochemical Society* 1943 **84** 83-96
[41] Bibinov N K, Fateev A A and Wiesemann K *Journal of Physics D-Applied Physics* 2001 **34** 1819-1826
[42] Bruggeman P and Brandenburg R *Journal of Physics D-Applied Physics* 2013 **46**
[43] Wei L, Lin W, Liao W, et al. *Journal of Electrostatics* 2022 **119** 103748
[44] Timo L, Juha T, Kauko J, et al. *Journal of Physics: Conference Series* 2011 **304** 012013
[45] Drimal J, Kozlov K V, Gibalov V I, et al. *Czechoslovak Journal of Physics* 1988 **38** 159-165
[46] Černák M, Hoder T and Bonaventura Z *Plasma Sources Science and Technology* 2020 **29** 013001
[47] Akishev Y S, Aponin G, Balakirev A, et al. *European Physical Journal D* 2011 **61** 421-429
[48] Synek P, Zemanek M, Kudrle V, et al. *Plasma Sources Science and Technology,* 2018 **27**
[49] Gibalov V I and Pietsch G J *Journal of Physics D: Applied Physics* 2000 **33** 2618-2636
[50] Raĭzer I U P *Gas Discharge Physics*: Springer-Verlag, 1991
[51] Bruins A P *Mass Spectrometry Reviews* 1991 **10** 53-77
[52] Huertas M L, Marty A M, Fontan J, et al. *Journal of Aerosol Science* 1971 **2** 145-150
[53] Hoppel W A and Frick G M *Aerosol Science and Technology* 1990 **12** 471-496
[54] Tigges L, Jain A and Schmid H J *Journal of Aerosol Science* 2015 **88** 119-134
[55] Alonso M and Alguacil F J *Aerosol and Air Quality Research* 2008 **8** 366-380
[56] Alonso M and Alguacil F J *Journal of Aerosol Science* 2003 **34** 1647-1664
[57] Mayya Y S and Sapra B K *Journal of colloid and interface science* 2002 **248** 283-294
[58] Gensdarmes F, Malet J, Boulaud D, et al. *Journal of Aerosol Science* 2000 **31** 614-615
[59] Cole C and Jones J E *Journal of Electrostatics* 2002 **56** 155-182

[60] Boeuf J P and Pitchford L C *Journal of Applied Physics* 2005 **97** 103307
[61] Boeuf J P, Lagmich Y and Pitchford L C *Journal of Applied Physics* 2009 **106** 023115
[62] Vaddi R S, Guan Y and Novosselov I *Journal of Aerosol Science* 2020 **148** 105587
[63] Ibarra I, Rodríguez-Maroto J and Alonso M *Journal of Aerosol Science* 2020 **140** 105479
[64] Chirokov A, Gutsol A, Fridman A, et al. *Plasma Chemistry and Plasma Processing* 2006 **26** 127-135
[65] Dong L F, Li X C, Yin Z Q, et al. *Chinese Physics Letters* 2001 **18** 1380-1382
[66] Natalia Yu B and Mark J K *Plasma Sources Science and Technology* 2014 **23** 065047
[67] Pujala U, Venkatesan S, Kumar A, et al. *Journal of Electrostatics* 2022 **117** 103713
[68] Borra J-P and Jidenko N "Device for controlling the charge of an aerosol in post-discharge": Centre National de la Recherche scientifique (CNRS) (3 rue Michel Ange, Paris, Paris, F-75016, FR) 2012.
[69] Babaeva N Y, Bhoj A N and Kushner M J *Plasma Sources Science and Technology* 2006 **15** 591-602
[70] Unger L, Boulaud D and Borra J P *Journal of Aerosol Science* 2004 **35** 965-979
[71] Profili J, Dap S, Levasseur O, et al. *Journal of Physics D: Applied Physics* 2017 **50** 075201
[72] Byeon J H, Hwang J, Hong Park J, et al. *Journal of Aerosol Science* 2006 **37** 1618-1628
[73] Jidenko N, Jimenez C, Massines F, et al. *Journal of Physics D-Applied Physics* 2007 **40** 4155-4163
[74] Brunet P, Rincon R, Margot J, et al. *Plasma Processes and Polymers* 2017 **14**
[75] Brunet P, Rincon R, Matouk Z, et al. *Langmuir* 2018 **34** 1865-1872
[76] Aouimeur D, Zouzou N, Miloua F, et al. *Journal of Physics: Conference Series* 2019 **1322** 012022
[77] Byeon J H, Ji J H, Park J H, et al. *Journal of Aerosol Science* 2008 **39** 460-466
[78] de La Verpilliere J L, Swanson J J and Boies A M *Journal of Aerosol Science* 2015 **86** 55-68
[79] Gunn R *Journal of Colloid Science* 1955 **10** 107-119
[80] Wiedensohler A *Journal of Aerosol Science* 1988 **19** 387-389
[81] Mathon R, Jidenko N and Borra J-P *Aerosol Science and Technology* 2017 **51** 282-291

Dielectric Barrier Discharge as bipolar ion source for aerosol charging: application to filtration, thin film, and aerosol size measurement

Nicolas Jidenko, Rémi Mathon, Valentin Gérard, Abdul Malik Adédiran and Jean-Pascal Borra.
Laboratoire de Physique des Gaz et des Plasmas, CNRS, Université Paris-Saclay, F-91405 Orsay, France

Supplementary information

1. Introduction

This supplementary information deals first with the experimental setup concerning post-DBD ion measurements then the mechanisms of ion losses are presented. Finally, post-DBD ion transport is examined through experimental results.

2. Experimental setup

2.1. Operating conditions

The flow rate of dry and filtered air is regulated from 0.3 to 8 L min^{-1} by a mass flow controller. The pressure in the DBD reactor is kept constant at 1020 mbar +/- 2 mbar. The gas velocity in the 1.7 mm gap DBD with L_{wall} =50 mm (cf. Figure S1) lies between 0.06 to 1.6 m.s^{-1}. The transit times in the discharge volume (the gas volume between metal electrodes) are between 68 to 2.6 ms and 85 to 3.2 ms in the post-discharge inter-alumina volume with L_{output} = 5 mm. Without discharge, the gas flow regime is laminar as the Reynolds number lies between 50 and 450 far below the transition value of 2000.

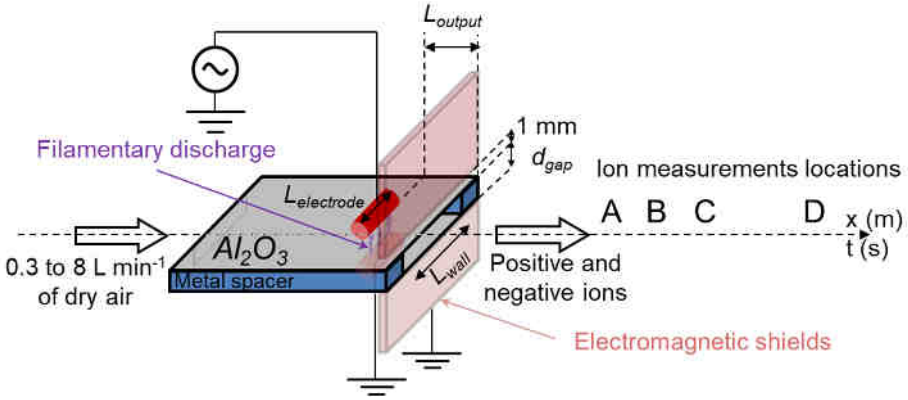

Figure S1. Scheme of DBD arrangement for post-discharge ion investigation

A sinusoidal high voltage is applied between metal electrodes. The choice of 60 kHz is the result of a compromise between better ion extraction at a higher frequency and higher power consumption and related surface and gas temperature that can alter aerosol in post-DBD (evaporation, melting, sintering). Using an oscilloscope with a bandwidth of 1 GHz, instantaneous applied voltage ($v(t)$) is measured with a high voltage probe (Tektronix P6015A), and discharge current in the external circuit ($i(t)$) is measured through a 25 Ω resistor. Input power (P, in Watt) is calculated by the integration of Lissajou's cycle ($q(v)$ obtained by replacing the 25 Ω resistor with a 1 nF capacitor cf. Figure 1). The capacitances of the DBD without plasma (C_{DBD}^{off} in F) and of the alumina plates ($C_{alumina}$ in F) can be determined with the smallest slope of the cycle [1].

The electrode and gas temperatures are measured with thermocouples. The time constant of DBD thermal equilibrium has been measured between 10 to 20 minutes depending on thermal conditions (i.e. gas flow rate in the DBD and around the DBD chamber that both control heat exchanges [2, 3]). All the measurements, presented here, have thus been performed at least 30 minutes after any modification of the operating conditions.

2.2. Post-DBD ion current measurements

In post-DBD, bipolar ions are separated by an electrostatic precipitator (ESP), made of two metal plates (70 × 70 mm) separated by 17.5 mm and polarised at 200 V. Ions current collected on the grounded plate is measured by an electrometer -Keithley 6010C or Keithley 6514 or Pegasor [4]-. Positive and negative currents are measured one after the other. Significant effort has been performed to ensure the representativeness of ion measurements. The ESP is shielded to limit electromagnetic disturbances of the power supply and the discharge. The mean transit time of the gas in the ESP (from 17 and 0.6 s for gas flow rates from 0.3 to 8 L min^{-1}) is much longer than the typical drift time of ions to the electrode (about 15 ms for ions with electrical mobility of 10^{-4} m^2 V^{-1} s^{-1}) to compensate space charge effects in the ESP and collect all ions. To reduce the influence of the electric field of the ESP on ions transport upstream of the ESP, a metal screen with a window is connected to the measurement electrode of ESP at the entrance of the ESP (cf. appendix 1).

As soon as the velocities of electric drift, diffusion, and thermophoresis can be neglected compared to the gas velocity, post-alumina ion densities, n_{ion} can be estimated from ion current measurements. As a first approximation, these conditions are fulfilled for a given set of operating conditions when the post-discharge ion current is negligible in the same operating conditions without gas flow. The mean post-DBD ion densities are derived from ions currents, gas flow rate, and ions unit charge:

$$n_{ion} = \frac{I_{ions}}{e.Q} \quad \text{(S3)}$$

with I_{ions} the positive or negative ion current (A); e = 1.6×10^{-19} C the elementary charge and Q the gas flow rate (m^3 s^{-1}). The measurements of positive and negative ion currents have been confirmed by aerosol size distribution measurement compared with well-established aerosol charging laws [5].

To investigate ion transport and losses, the measured ion densities along post-DBD have been compared to theoretical ion losses. Ions currents have been measured at five locations in the post-discharge (referred to as A, B, C, D, and E with the ESP located at 9, 12.5, 17, 50, and 100 mm from the center of the discharge respectively, cf. Figure S1). The volumes crossed by the gas before ion measurement are 1.4, 2.5, 4, 8.5, and 90 cm^3 from A to E. Measurements at E are carried out downstream of the ESP using a second ESP that allows us to confirm the collection efficiency of the first ESP.

Theoretical ion losses are estimated for each physical process separately (diffusion, recombination, and electrostatic repulsions) using empirical or theoretical laws (cf. section 3). The three volumes of interest are the "discharge volume" defined as the volume of the gas layer between metal electrodes, the post-discharge inter-alumina, and the post-alumina volumes. The ion penetration is defined as the ratio of the ion densities at the outlet of a given volume to the ion density at the inlet.

3. Calculation of ion losses

Empirical or theoretical laws for ion penetration related to diffusion, ion recombination, and electrostatic losses by self-repulsion to the wall as described below.

a) Diffusion losses are estimated from the empirical law [6]. This law has been validated for aerosol particle diameter as small as that of typical air ions, in tubes within 1% valid for [7].

$$P_{diff} = 1 - 5.50\mu^{\frac{2}{3}} + 3.77\mu \quad for\ \mu < 0.007$$
$$= 0.819\exp(-11.5\mu) + 0.0975\exp(-70.1\mu) + 0.0325\exp(-179\mu) \quad for\ \mu > 0.007 \quad \text{(S4)}$$

with $\mu = \frac{D \cdot L \cdot W}{Q \cdot h}$; D, the diffusion coefficient; L the tube length, W the width of the plates, h the distance between the plates and Q the gas flow rate.

The diffusion coefficients are calculated from Einstein's relation from ion mobility (Z^+ = 1.4×10^{-4} m^2 V^{-1} s^{-1} and Z^- = 1.7×10^{-4} m^2 V^{-1} s^{-1} [8]) leading to D^+ = 3.5×10^{-6} m^2 s^{-1} and D^- =4.3×10^{-6} m^2 s^{-1}) for positive and negative ions respectively.

b) Ion-ion recombination: Ion penetration due to ion-ion recombination (P_{recomb}) is calculated with the smallest value between n_{ion}^+ and n_{ion}^-, assuming the same profiles for positive and negative ion density, using:

$$P_{recomb}(t) = \frac{1}{1+\alpha \cdot N_0 \cdot t} \quad \text{(S5)}$$

with P_{recomb} the ion penetration, N_0 initial ion density (m^{-3}), α recombination coefficient (1.6×10^{-6} $cm^3.s^{-1}$ at 18°C [9, 10]) and t the time (s).

c) *Electrostatics losses:* there are two electrostatics cases, the ion losses on the wall by self-electrostatics repulsion and by the decreasing oscillating external field due to the polarization of the DBD electrodes neglecting the surface electric field.

- Ion density decay by self-repulsion has been studied by Whitby [11]:

$$P_{self-repulsion}(t) = \frac{1}{1+N_0 \frac{e.\mu_{ion}}{\varepsilon_0} t} \quad \text{(S6)}$$

This law is valid only for unipolar ions with an ion density profile only controlled by self-repulsion. In post-DBD, bipolar ion profiles are probably not flat as the oscillating electric field at 60 kHz still affects ion trajectories. Nevertheless, this law can be used as a first approximation to estimate the decay of positive ion densities that are in excess.

- *The oscillating electric field*, in the post-discharge inter-alumina volume, Laplace, and surface electric fields partly collect ions on the alumina plates. Calculations for aerosol deposition have been reported [12, 13]. Nevertheless, due to many approximations on the electric field, no ion penetration equation is used in this paper.

4. Ion transport controlled by EHD equilibrium (ΔU_{pp}, Q)

Post-DBD ion currents (I_{ions}) are measured for different applied voltages and gas flow rates to confirm that ions transport is controlled by a competition between electrostatic and hydrodynamic forces.

4.1. Applied voltage

Positive and negative post-DBD ion currents measured after a transit time of 42 ms are plotted as a function of the overvoltage ΔU_{pp}, with an alumina length downstream the discharge, L_{output} of 10 mm in Figure S2(a) and of 25 mm in Figure S2(b) (for a 1 mm discharge gap, at 4 L min^{-1} gas flow rate). The vertical lines define the voltage ranges (I, II, and III) with 1, 2, or 3 curtains of DF and the transitions between these voltage ranges (I→II and II→III) (cf. section 3.1).

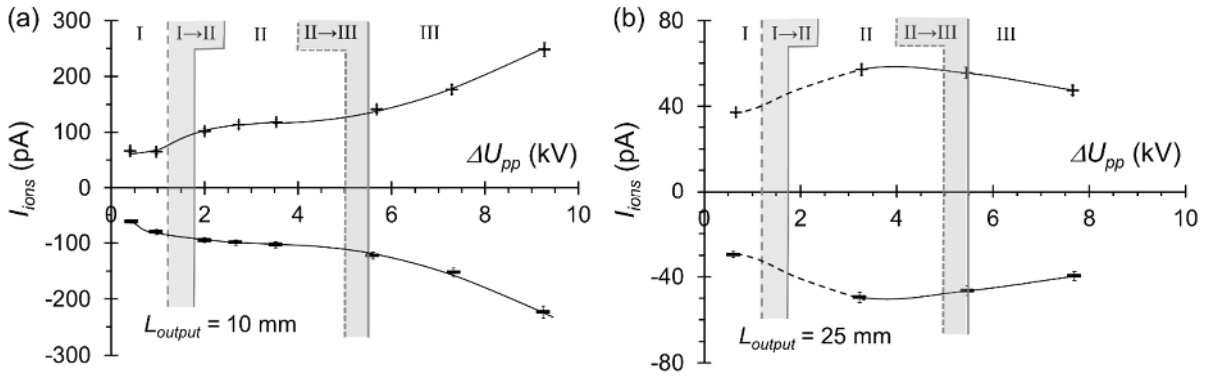

Figure S2. Post-DBD ion currents measured at D versus overvoltage for a 1 mm DBD gap, air flow rate of 4 L min^{-1}, L_{wall} = 36 mm and alumina length downstream the DBD, L_{output} of (a) 10 mm with a 42 ms transit time between discharge and ion measurements and (b) 25 mm with a transit time of 49 ms.

In Figure S2, positive and negative post-DBD ion currents (I_{ions}) follow the same trends. Positive post-DBD ion currents exceed by 10-20% negative ones. Lighter and more mobile negative ions are more easily lost on the walls than positive ones. Moreover, positive and negative ions are produced at different times and/or locations: by ionization in high electric field for positive ions and by attachment of electrons in low electric field for negative ones that could account for the discrepancies.

In Figure S2 (a), post-DBD positive and negative ion currents rise with increasing applied voltage. Higher applied voltage leads to more numerous DF that develop in the DBD per time unit (i.e. more numerous sources of ion). Once produced, most of the charges are collected on the dielectric surfaces in the discharge volume. About 10^{-5} % of the charges are extracted from the discharge (discharge current between 0.4 and 7.2 mA for ion current between 40 and 300 pA). The ion production efficiency (defined as the ratio of post-discharge ion current to discharge current, not presented) declines with increasing applied voltage, due to the electro-collection of ions in the post-discharge inter-alumina volume as confirmed in section 4.4.

The number of DF curtains affects the evolution of post-DBD ion currents as a function of the applied voltage DF (see Figure S2a). After the propagation of a DF, positive and negative ions are slowly separated by the electric field until the field reverses [14] and radially expands around the DF [15, 16]. Moreover, ions undergo surface and volume electric fields related to DFs that develop around them. The intensity of these interactions depends on the spatial and temporal distributions of the surrounding DF. For ΔU_{pp} below 2 kV, the ion currents increase with the applied voltage i.e. with the number of DF that develops on a single curtain of DF. With 2 DF curtains, the post-discharge current is nearly constant despite an increasing number of DF. DF. The downstream curtain of DF probably acts as an electrostatic wall for ions produced by the upstream curtain limiting the ion extraction from the discharge volume. Moreover, the increase in the amplitude of the Laplace electric field enhances the electro-collection of ions on alumina plates. The electric field is retro-controlled by the surface electric field which most probably limits electro-collection enhancement in the discharge volume. Nevertheless, the Laplace field increases beyond the discharge volume that favors ion electro-collection on alumina plates in the post-discharge inter-alumina volume. With 3 DF curtains, post-discharge ion currents increase as a quadratic function of the applied voltage most probably due to thermal effects as discussed in section 4.5.

In Figure S2 (b), the drastic reduction of post-discharge ion currents compared to Figure S2 (a) exhibits the critical role of the length of the alumina plate downstream of the discharge in terms of ion losses. The increase in Al_2O_3 length of a factor of 2.5 leads to a reduction in post-DBD ion current by a factor of 1.3 to 5 depending on the applied voltage. The most surprising fact is that the evolution of post-DBD ion currents with the applied voltage presents a maximum for the 25 mm L_{output}. The lower post-discharge ion currents at higher applied voltage tends to support that electro-collection controls ion density in the post-discharge inter-alumina volume (cf. section 4.4).

4.2. Gas flow rate

The post-DBD ion currents and the ratio of positive to negative ion currents are plotted as a function of the gas flow rate between 0.5 and 8 L min^{-1} for ΔU_{pp} = 1 kV with the ESP at location C in Figure 4 (a). The evolutions of negative ion currents versus gas flow rate for ΔU_{pp} of 1.3, 1.7, 2.7, and 4.6 kV with ESP at A are represented in Figure 4 (b).

Figure S2 and Figure 4 confirm the results already reported by Bourgeois et al. downstream a plane-to-plane DBD after a 4 mm diameter tube with a length of 50 mm (leading to 6 - 100 ms transit time) at a constant gas temperature of 313 K [8]. Positive and negative ion currents follow the same trends with an excess of positive ions that can be tuned by the gas flow rate (cf. I_{ion}^{+}/I_{ion}^{-} in Figure 4 (a)) and applied voltage.

Positive to negative ion currents ratio I_{ion}^{+}/I_{ion}^{-} can be correlated to aerosol mean charge and gives useful data on ion losses. Assuming that I_{ion}^{+}/I_{ion}^{-} is an estimation of N_{ion}^{+}/N_{ion}^{-}, one can define the critical parameter that controls the mean charge of aerosol in a bipolar ion environment $N_{ion}^{+}Z_{ion}^{+}/N_{ion}^{-}Z_{ion}^{-}$ [17]. The ratio Z_{ion}^{+}/Z_{ion}^{-} can be calculated from ion mobility measurements and lies in the range of 0.6 to 1.05 [8]. Moreover, recombination or/and Brownian diffusion controls ion losses if I_{ion}^{+}/I_{ion}^{-} is higher than 1 and increases with the transit time. If the ratio I_{ion}^{+}/I_{ion}^{-} tends to 1 electrostatic repulsion are dominant. In Figure 4 (a), the non-monotonous evolution of I_{ion}^{+}/I_{ion}^{-} proves that the dominant mechanism of ion losses depends on the gas flow rate and the related distribution of ion clouds.

In Figure 4 (b), each curve presents a minimum value with a transition gas flow rate that depends on the applied voltage. Above the transition gas flow rate (e.g. 2.5 L min^{-1} at ΔU_{pp} = 4.5 kV), ion currents increase with the gas flow rate due to the reduction of the transit time and the subsequent reduction of ion losses. Moreover, a larger gas flow rate leads to higher ion dilution reducing ion losses by ion-ion recombination. Below the transition gas flow rate, ion currents increase with the reduction of the gas flow rate, much more than previously reported. The measurements are carried out closer to the discharge than in previous results: only 9 mm downstream of the DBD instead of 50 mm for Bourgeois et *al.*. *The 50 mm length tube probably enhances ion-ion recombination which lessens the discrepancies.* Moreover, previous data were obtained at constant gas temperature whereas the data presented here are at quasi-steady thermal equilibrium. The increase in ion currents with increasing applied voltage and decreasing gas flow rate is most probably due to more efficient diffusion mechanisms at low gas flow rates and limited ion-ion recombination. As the transition gas flow rate depends on the applied voltage, it is most probably related to a transition in the gas flow regime (from laminar to turbulent gas flow) induced by DF despite the laminar flow regime in the DBD without discharge (Reynolds number < 2000). Each DF generates ion wind and temperature gradients. The collective effect increases with the number of DF tuned by the applied voltage. Moreover, a higher number of DF leads to higher surface temperature and potential turbulences by convection. The turbulent mixing favors the homogeneous distribution of positive and negative ions and thus ions losses by ion-ion recombination.

To summarize, those data confirm that the transport of ions in post-DBD is the result of a competition between electro-collection and hydrodynamics forces (advection) with active ion-ion recombination.

4.3. Ion-ion recombination in post-alumina volume

To show that ion-ion recombination mainly controls ion density decay along post-alumina volume, post-DBD ion currents have been measured at three locations for three operating conditions (cf. Figure S3(a)) and compared with ion-ion recombination theory. The measured ion currents decrease along post-discharge with a stronger decay of positive current than negative one, due to space charge repulsion related to the excess of positive ion. Therefore, only negative ion densities are thus plotted as a function of the gas transit time from the discharge for ΔU_{pp} = 1.5 kV and compared with ion-ion recombination law in Figure S3 (b) for 0.3 and 4 L min^{-1}.

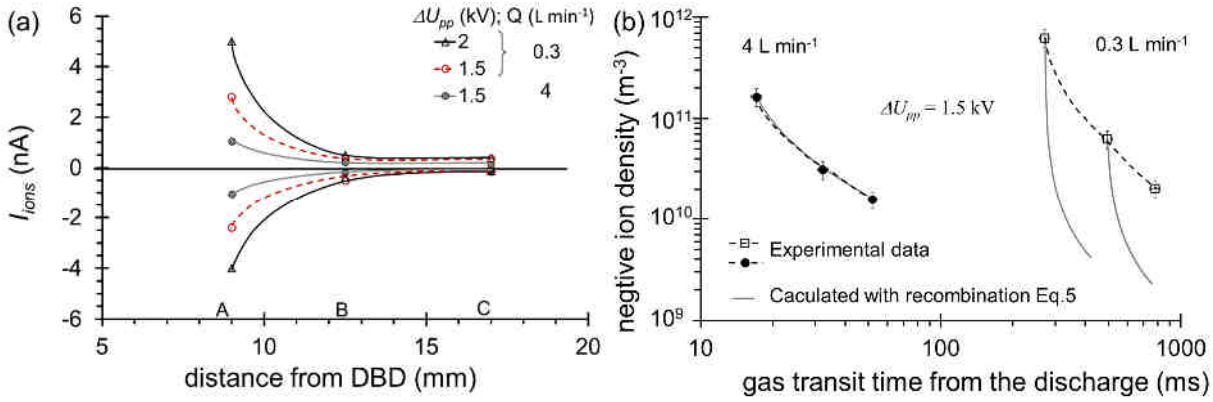

Figure S3. (a) Evolution of positive and negative post-DBD ion currents for ΔU_{pp} = 1.5 and 2 kV, at 0.3 and 4 L min^{-1} for the 1.6 mm gap DBD with L_{output} = 5 mm, L_{wall} = 50 mm (b) negative ion density (same data for U_{pp} = 1.5 kV) compared with theoretical ion decay by ion-ion recombination from Eq.5.

In Figure S3 (b), the decay of negative ion density at 4 L min^{-1} (v_{gas} = 0.83 m s^{-1} between alumina plates) agrees with the theoretical decay by ion-ion recombination. It proves that, in these conditions, negative and positive ion density profiles are the same within a few percent, and both electric fields and ionization in the post-alumina volume can be neglected. At a high flow rate above 4 L min^{-1}, the negative ion density decay is thus controlled by ion-ion recombination and losses by self-repulsion and diffusion are negligible.

At 0.3 L min^{-1} (v_{gas} = 0.063 m s^{-1} between alumina plates), the post-DBD ion density decreases less than expected by recombination. Neglecting post-DBD ionization, the discrepancies can arise from: (i) an overestimation of the measured ion density (related to ion velocity higher than gas velocity), (ii) a reduction of the recombination coefficient with the rise of the gas temperature, and (iii) a separation of positive and negative ions in space that reduces ion losses by recombination. The two first combined effects only explain about 10 % of the discrepancies at 0.3 L min^{-1}. Thermal diffusion of ions (thermophoresis) is negligible at a thermal steady state in the post-alumina volume. Electric drift parallel to the gas flow can lead to a reduction of ion density by a factor of 2 in the worst case as the electric drift velocity has to be negligible compared to 0.83 m s^{-1} (gas velocity at 4 L min^{-1}). The gas temperature can reach 320 K leading to a reduction of 25% of the recombination coefficient. Thus, these results tend to show that the separation of positive and negative ions in space leads to an efficient transport of bipolar ions with reduced ion recombination at low gas velocity. Even if recombination is less effective than expected, it remains the dominant mechanism of negative ion decay.

4.4. Electro-precipitation in post-discharge inter-alumina volume

To investigate ion losses in the post-discharge inter-alumina volume, positive ion currents are measured for 3 lengths of alumina plates downstream of the discharge (L_{output} = 10, 25, and 40 mm) for a given operating condition (d = 1 mm, ΔU_{pp} = 5.4 kV, I_d = 5.3 mA, Q = 4 L min^{-1}, L_{wall} = 36 mm) location D). The aim is to estimate the ion current decay in the post-discharge inter-alumina volume. To do so, we assume that the post-DBD ion currents measured for different lengths of alumina plates can be used.

Positive ion currents are plotted versus post-discharge transit time from 42 to 56.5 ms controlled by L_{output} at 4 L min^{-1} in Figure S4(a). The gas flow rate has been chosen because ion recombination controls ion densities in the post-alumina volume (cf. §4.3). Post-DBD ion current at the exit of the alumina plates can thus be estimated from the measured post-DBD ion currents using Eq. 5. These calculated currents are plotted versus the transit time in the DBD with the largest alumina plate downstream the discharge and compared to theoretical laws for each process of ion losses in Figure S4 (b). Theoretical post-DBD ion currents are calculated for each process of ion losses using equations (S4) to (S6). Homogeneous mixing of positive and negative ions is assumed for recombination calculations. The net space charge density (20% of the positive ion density) is taken into account for positive ion losses by self-repulsion. The theoretical evolution of ion current including all processes, neglecting the coupling between these processes, is plotted in the black full line in Figure S4 (b).

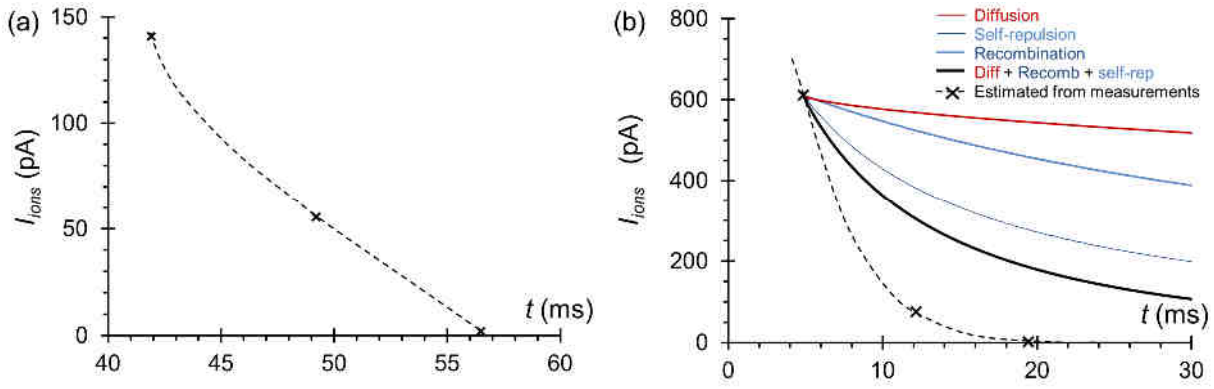

Figure S4. Positive post-DBD ion currents (a) measured for 3 alumina plate lengths versus transit time from the discharge up to ion measurement, Lwall = 36 mm, ESP at D (b) estimated from ion currents measurements and calculated theoretical ion currents evolutions from Eq. (5, 6 and 7) versus transit time in the post-discharge inter-alumina volume.

In Figure S4 (a), I_{ion} decreases by 2 orders of magnitude with transit time from 42 to 56.5 ms. The length of the alumina plate is the most critical parameter that affects post-alumina ion current in the post-discharge inter-alumina volume. In Figure S4(b), none of the considered ion losses mechanism alone can explain such a fast decay. Diffusion is negligible and recombination only accounts for half of the ion current decrease after 30 ms transit time. All processes together, neglecting the couplings between these processes, represent two-thirds of the ion current decay. Whatever the ion mixing dynamics is, another mechanism is thus involved to account for the results. Electro-collection related to Laplace and surface electric field is most probably the dominant mechanism of ion losses in the post-discharge inter-alumina volume. Rough calculations of ion losses by electro-collection assuming a sinusoidal electric field with an amplitude of 10^6 V m^{-1} as defined in [13], with homogeneous ion density and neglecting surface polarisation leads to ion current decay faster than the measured ones. These calculations and the influence of alumina length on I_{ion} (see §4.1) both tend to support that electro-collection on dielectric surfaces mainly controls the decrease of ion densities in the post-discharge inter-alumina volume.

4.5. Ion extraction from the discharge volume

To investigate the extraction of ions from the discharge volume, post-DBD positive ion currents are measured downstream three DBD with discharge gaps of 0.5, 0.9, and 1.7 mm, at 4 L min^{-1} and L_{output} = 10 mm (cf. Figure S5). The vertical lines define the voltage ranges with 1, 2, or 3 curtains of DF, as defined in the section. A larger discharge gap leads to a higher charge per DF with less numerous DF per unit time and area, at constant discharge current. Moreover, a constant discharge current for a larger discharge gap implies higher input power and higher electrode temperature. For example, at I_d = 6 mA, the input power is 10 W, and the electrode temperature is 75°C for the 0.5 mm gap DBD and for the 1.7 mm gap DBD, 12 W and 95 °C. So that for the same production of charge per second in the DBD, both the spatiotemporal distribution of ions and the temperature profile are affected by the modification of the discharge gap length.

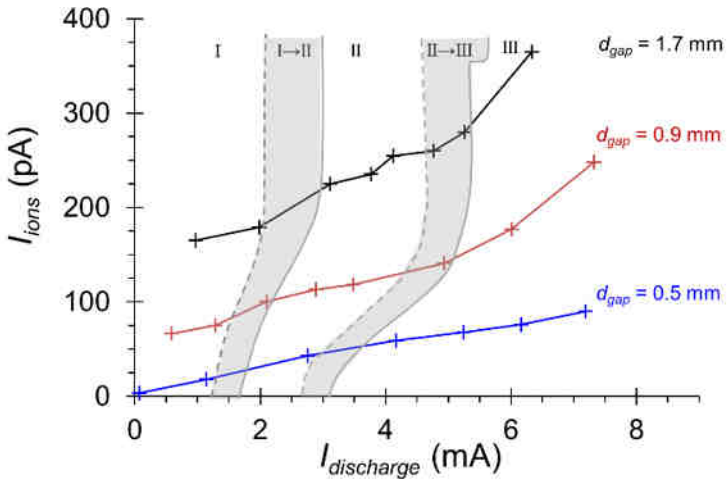

Figure S5. Post-DBD ions currents for three discharge gap lengths (0.5, 0.9, and 1.7 mm) as a function of $I_{discharge}$ at Q = 4 L min^{-1} for L_{output} = 10 mm and ESP at D transit times between 40 and 46 ms.

The results of section 4.1, concerning the influences of the number of DF per unit time and area and the number of DF curtains on post-DBD ion currents (I_{ion}), are confirmed for each discharge gap in Figure S5.

At constant discharge current (I_d) and gas flow rate, higher I_{ion} are measured at increasing gap length. A factor of 3.4 on the gap length (from 0.5 to 1.7 mm) leads to an increase in I_{ion} by a factor between 3 and 10 depending on I_d. This effect is due to reduced losses in the discharge and the post-discharge inter-alumina volumes despite longer transit time from the discharge up to the ion current measurements. In the DBD, coupled heat and mass transfers are enhanced by electro-hydrodynamics effects. After showing that a modification of the gap length at constant I_d has a negligible effect on ion recombination, we will prove that both electric drift and thermophoresis are involved in the reduction of ion losses at increasing discharge gap length.

As a first approximation, neglecting the modification of ion distribution in space and time, the variation of the discharge gap length has a negligible effect on ion losses by recombination. The variation of the transit time (from 40 to 46 ms for 0.5 and 1.7 mm gap lengths respectively) is partly compensated by the reduction of the recombination coefficient with the gas temperature (from 75°C to 95 °C). For example, at I_d = 6 mA, the theoretical discrepancies of ion currents related to ion recombination are only of 2% for gap lengths of 0.5 and 1.7 mm.

Ion losses are mainly controlled by electro-collection between alumina plates. A larger discharge gap length favors ion extraction and limits electro-collection just after ion production and during the post-production transit in the DBD gap. The increase in the gap length, at constant I_d and Q, increases (i) the mean drift length for the ions to be collected, (ii) the local surface charge deposition on the feet of the DF, (iii) the temperature in the DBD and (iv) the density and temperature gradients around DF that enhance heat and mass transfers from the DF to the surrounding gas. After the junction of the DF with the surface, the higher surface electric field at a larger gap length repels more strongly in the gap the ions approaching the dielectric surface. Moreover, the higher surface temperature at a higher gap length reduces alumina surface conductivity and thus the radial spreading of surface charges from each DF that reinforces the reduced electric field on the DF axis before the change in polarity [8]. Finally, the temperature gradient in the gas close to alumina surfaces limits ion collection by thermophoresis.

The effects of the surface electric field, as well as diffusion and temperature gradients around DF, have been confirmed by ion current measurement with a gas counter-flow (from the ESP to the discharge). From these results, a bipolar ion source with limited effluents produced by the DF (O_3, NOx, and nanoparticle) has been patented [18].

References

[1] Bruggeman P and Brandenburg R *Journal of Physics D-Applied Physics* 2013 **46**

[2] Jidenko N, Bourgeois E and Borra J P *Journal of Physics D: Applied Physics* 2010 **43**

[3] Svarnas P, Papadopoulos P K, Athanasopoulos D, et al. *Journal of Applied Physics* 2018 **124** 13

[4] Timo L, Juha T, Kauko J, et al. *Journal of Physics: Conference Series* 2011 **304** 012013

[5] Mathon R, Jidenko N and Borra J-P *Aerosol Science and Technology* 2017 **51** 282-291

[6] Gormley P G and Kennedy M *Proceedings of the Royal Irish Academy. Section A: Mathematical and Physical Sciences* 1948 **52** 163-169

[7] Alonso M, Kousaka Y, Hashimoto T, et al. *Aerosol Science and Technology* 1997 **27** 471-480

[8] Bourgeois E, Jidenko N, Alonso M, et al. *Journal of Physics D: Applied Physics* 2009 **42** 205202

[9] Hoppel W A and Frick G M *Aerosol Science and Technology* 1990 **12** 471-496

[10] Bricard J, Cabane M and Madelaine G *Journal of Colloid and Interface Science* 1977 **58** 113-124

[11] Whitby K T *Rev. Sci. Instrum.* 1961 **32** 1351-1355

[12] Profili J, Dap S, Levasseur O, et al. *Journal of Physics D: Applied Physics* 2017 **50** 075201

[13] Jidenko N and Borra J-P *J. Phys D.: Apply Phys* 2005 **38** 617-620

[14] Fridman A, Gudsol A and Cho Y I "Non-Thermal Atmospheric Pressure Plasma" *Advances in Heat Transfer: Transport Phenomena in Plasma*: Elsevier Science 2007.

[15] Xu X D P and Kushner M J *Journal of Applied Physics* 1998 **83** 7522-7532

[16] Natalia Yu B and Mark J K *Plasma Sources Science and Technology* 2011 **20** 035017

[17] Gunn R *Journal of Colloid Science* 1955 **10** 107-119

[18] Borra J-P and Jidenko N "Device for controlling the charge of an aerosol in post-discharge": Centre National de la Recherche scientifique (CNRS) (3 rue Michel Ange, Paris, Paris, F-75016, FR) 2012.